Exciton Coherence and Energy Transport in the Light-Harvesting Dimers of Allophycocyanin

Jordan M. Womick and Andrew M. Moran*

Department of Chemistry, The University of North Carolina at Chapel Hill, Chapel Hill, North Carolina 27599

Received: August 7, 2009; Revised Manuscript Received: October 12, 2009

Femtosecond transient grating and photon echo spectroscopies with a sub-20 fs time resolution are applied to allophycocyanin (APC), a protein located at the base of the phycobilisome antenna of cyanobacteria. Coupling between pairs of phycocyanobilin pigments with nondegenerate energy levels gives rise to the four-level exciton electronic structure of APC. Spectroscopic signals obtained in multiple experiments (e.g., linear absorption, fluorescence, transient grating, 2D Fourier transform photon echo) are used to constrain the parameters of a Frenkel exciton Hamiltonian. Comparison between experiment and theory yields a robust microscopic understanding of the electronic and nuclear relaxation dynamics. In agreement with previous work, transient absorption anisotropy establishes that internal conversion between the exciton states of the dimer occurs with time constants of 35, 220, and 280 fs. The sub-100 fs dynamics are decomposed into three distinct relaxation processes: electronic population transfer, intramolecular vibrational energy redistribution, and the dephasing of electronic and nuclear coherences. Model calculations show that the sub-100 fs red-shift in the transient absorption signal spectrum reflects interference between stimulated emission (ESE) and excited state absorption (ESA) signal components. It is also established that the pigment fluctuations in the dimer are not well-correlated, although further experiments will be required to precisely quantify the amount of correlation. The findings of this paper suggest that the light harvesting function of APC is enhanced by nondegeneracy of the pigments comprising the dimer and strong vibronic coupling of intramolecular modes on the phycocyanobilins. We find that the exciton states are 96% localized to the individual molecular sites within a particular dimer. Localization of the transition densities, in turn, is suggested to promote significant vibronic coupling which serves to both broaden the absorption line shape and open channels for fast internal conversion. The dominant internal conversion channel is assigned to a promoting mode near 800 cm^{-1} involving hydrogen out-of-plane (HOOP) wagging motion similar to that observed in phytochrome and retinal. This rate enhancement ensures that all photoexcitations quickly and efficiently relax to the electronic origin of the lower energy exciton state from which energy transfer to the reaction center occurs.

I. Introduction

Underlying photosynthetic light harvesting is a complicated world of fluctuating nuclei whose amplitudes, rates, and many-body correlations govern the fate of electronic excitations.[1–3] It is well-established that interactions between pigments and the surrounding environment (e.g., protein matrix, aqueous solvent) span a range of strengths and time scales.[4–6] Spatially correlated environmental fluctuations add a particularly rich dimension to the picture.[7–13] Correlations in the environment-induced fluctuations of energy gaps and couplings in systems composed of multiple pigments can, in principle, range from full correlation to full anticorrelation. The complexity of this phenomenon challenges modern experimental techniques and theory. Nonetheless, the impact of correlated dynamics can be substantial and has been found to boost the contribution of coherent light harvesting mechanisms by 20% in the Fenna−Matthews−Olson protein.[10] Further theoretical and experimental investigations are required to fully understand how biological antennae use correlations to enhance function. This understanding will likely apply to artificial systems.[14,15]

Correlated dynamics influence energy transfer kinetics in both weak and intermediate coupling regimes. Recent work illustrates how correlated excited state (i.e., exciton) energy level fluctuations give rise to recurrences in energy transfer.[15–17] These recurrences reflect partially correlated fluctuations at the donor and acceptor sites, where the requirement for partial correlation can be understood with consideration of two well-defined limits. In the strong coupling limit, full energy donor and acceptor correlation manifests as "Rabi-like" oscillations in electronic populations, whereas irreversible relaxation takes hold when coupling between the donor and acceptor is weak compared to the system−bath interaction strength. It is also important to recognize that donor and acceptor units can possess internal structure whose dynamics can influence energy transfer kinetics through correlated line broadening.[18–21] That is, the spectroscopic line shapes entering Förster's rate formula generally reflect the extent to which spatially correlated dynamics occur within the molecular complexes comprising the donor and/or acceptor units.[22] Nonlinear spectroscopies have proven useful for uncovering many aspects of line broadening,[23,24] whereas spatial correlations remain elusive due to their complex many-body nature.[25,26] Advances in the understanding of correlated line broadening will require the application of specialized experimental techniques to appropriate model systems.[22,27]

In this paper, we investigate photoinduced relaxation dynamics in allophycocyanin (APC) using transient grating and photon echo spectroscopies. Signals are analyzed using a theoretical model to obtain the parameters of a Frenkel exciton Hamiltonian. APC is a particularly good model for the study of exciton dynamics because of its well-defined geometry and electronic structure.[28–30] Figure

---

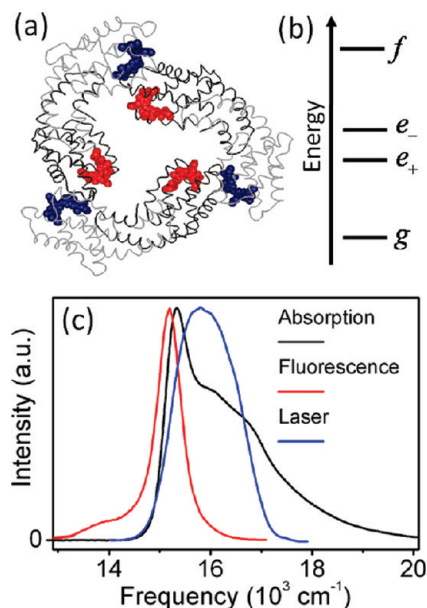**Figure 1.** (a) Structure of APC trimer in which blue and red, respectively, signify α84 and β84 subunits. (b) Each pigment dimer possesses four-level exciton electronic structure. (c) Absorption (black) and fluorescence emission (red) spectra of APC. Overlaid in blue is the spectrum of the 15 fs laser pulse used in this work.

1 shows that the X-ray crystal structure of APC possesses a 3-fold axis of symmetry consisting of three dimers with phycocyanobilin pigments separated by 2.1 nm.[31] Pairs of dimers interact weakly because they are separated by distances of approximately 5 nm. Thus, to a good approximation, coupling between pairs of phycocyanobilins transforms the electronic structure into an "exciton" basis consisting of four levels, where the linear absorption spectrum presented in Figure 1c corresponds to transitions between the ground state and the two single exciton levels. The peak at 15 300 cm^{-1} predominantly represents the lower energy transition to $e+$, whereas the higher energy transition to $e-$ appears as a broad "shoulder" centered at 16 200 cm^{-1}. Although vibronic structure is not well-resolved in the linear absorption spectrum, this paper will show that vibronic coupling is essential to fitting the absorption line shape and also to the description of internal conversion between exciton states. For example, a significant portion of the intensity underneath the 16 200 cm^{-1} band is associated with the Franck–Condon progression of the $e+$ transition if the fluorescence spectrum is taken to be the mirror image of the $e+$ absorption line shape;[32] mirror image symmetry assumes identical vibronic structure for the absorption and fluorescence spectra (i.e., equivalent normal modes and vibrational frequencies for the ground and excited states).[6,33]

Spectroscopic signatures of correlated line broadening are difficult to ascertain. In principle, the analysis of two-dimensional photon echo line shapes measured at a fixed population time is a direct route to uncovering these dynamics.[18-22] However, interference between transitions (i.e., spectral overlap) prevents this approach for most pigment complexes because energy gaps between the multiple exciton levels are generally comparable to the spectroscopic line widths. Alternative approaches first prepare coherent superpositions of electronic states, then monitor the loss of correlation in the time domain (e.g., pump–probe anisotropy).[9,14,17,22,34-39] The rate of decoherence for a pair of excitons generally increases with decreasing exciton correlation. In essence, the instantaneous distribution of energy gaps in an ensemble broadens in the absence of correlation; fast damping is the natural outcome of superposing

many oscillators with incommensurate frequencies. Here we examine signatures of correlated line broadening encoded in the dephasing rates of photoexcited coherent superposition states. Correlation within the dimer of APC is quantitatively evaluated with the support of a theoretical model.

Beck and co-workers have investigated femtosecond dynamics of APC with a variety of four-wave mixing spectroscopies.[28,32,40,41] It was firmly established that the 15 300 and 16 200 cm^{-1} absorption bands in APC correspond to exciton states associated with the phycocyanobilin dimers. Pump–probe anisotropy experiments found that internal conversion between exciton states occurs with time constants of 30–56 and 280 fs,[28] whereas photon echo spectroscopy identified an additional 220 fs relaxation process.[41] Subpicosecond red-shifting of the transient absorption signal spectrum was attributed to inertial solvation processes and relaxation within the manifold of photoexcited intramolecular nuclear coordinates (i.e., vibrational cooling).[40] Of particular relevance to the present paper is the suggestion of imperfect correlation between exciton states discussed in ref 41. Technical advances in nonlinear optics and spectroscopic techniques occurring in the past decade now allow this issue to be more carefully examined here.

Strong vibronic coupling of a large number of intramolecular modes is known to occur with APC[42-44] as well as other phycobiliproteins.[45-47] Resonance Raman experiments observe a large number of transitions in the vibrational fingerprint region.[43,44] In addition, the analysis of earlier pump–probe measurements performed with 16 fs pulses yielded large Huang–Rhys factors for several vibrations.[42] The strong vibronic coupling observed in these experiments reflects the displacement of equilibrium nuclear coordinates for the ground state compared to the single exciton states. However, efficient internal conversion between $e-$ and $e+$ requires that significant geometric distortion occurs in the transition between excited states. Below we suggest that a promoting mode near 800 cm^{-1} assists in the subpicosecond internal conversion of APC because the energy gap between the $e+$ and $e-$ exciton states exceeds the characteristic frequency of overdamped nuclear motion in the bath (i.e., spectral density).

II. Experiment

Allophycocyanin (APC) was purchased from Prozyme as a suspension in 60% ammonium sulfate. Spectroscopic measurements used solutions of APC in 100 mM potassium phosphate buffer at pH 7.0. All experiments were performed within 12 h of solution preparation. Optical experiments circulated the solutions at a rate of 10 mL/s in a flow system using a peristaltic pump with reservoir of 10 mL. The absorbance of the solution was 0.15 at 15 300 cm^{-1} in the 0.5 mm path length flow cell. Absorbance spectra were measured before and after optical experiments to confirm the absence of sample degradation.

Transient grating (TG) and photon echo (PE) experiments utilize a Quantronix Integra C Titanium Sapphire amplifier producing 800 nm, 120 fs laser pulses at 1 kHz. The laser system pumps a home-built noncollinear optical parametric amplifier (NOPA) yielding pulses with spectra spanning 500–750 nm. The portion of the full spectrum shown in Figure 1c is obtained by filtering the higher and lower frequency spectral content in a fused silica prism compressor. Pulses are compressed to 15 fs duration and characterized using transient grating frequency resolved optical gating.[48]

TG and PE experiments are performed using the same passively phase-stabilized, diffractive optic-based interferometer for which a detailed description is given in ref 22. The

Light-Harvesting Dimers of Allophycocyanin

J. Phys. Chem. B, Vol. xxx, No. xx, XXXX **C**

interferometer design resembles those reported in several earlier publications.[49−57] Briefly, a boxcar (i.e., square) laser beam geometry is used to generate a signal in the $\mathbf{k}_S = -\mathbf{k}_1 + \mathbf{k}_2 + \mathbf{k}_3$ phase matched direction. All three pulses and a local oscillator field are derived from the same NOPA. Times at which the E_1 and E_2 pulses arrive at the sample are varied by inserting independent prism wedges in the paths of both beams, whereas a conventional optical delay line controls the arrival of the E_3 and local oscillator pulses. The E_3 and local oscillator pulses pass through an identical pair of prism wedges to ensure that all four pulses possess identical dispersion. Pulses with energies of 5 nJ are focused to a 120 μm spot size at the sample for a fluence of 1.4×10^{14} photons/cm^2. Increasing the pulse energies by a factor of 4 has no effect on the measured dynamics. Signals are detected using spectral interferometry with a back-illuminated CCD array (Princeton Instruments PIXIS 100B) mounted on a 0.3 m spectrograph (Princeton Instruments). Integration times are $100-200$ ms. A Fourier transform algorithm is used to process the measured interferograms.[52,53,58−60]

The TG signals presented here represent the average of 15 scans of the optical delay line. Anisotropies compare tensor elements for real (absorptive) signal components measured in immediate succession, where data acquisition for one tensor element requires approximately 25 min. The experiments were repeated several times and suggest that this procedure yields an error of approximately $\pm$ 0.03 in the anisotropy. PE scans acquire two-dimensional spectra at a series of population times, T, as described in ref 22. Rephasing and nonrephasing signals are superposed to obtain absorptive spectra.[60,61] Scans of photon echo spectra at a series of population times are repeated 10 times and averaged for a total data acquisition time of 5 h.

The real and imaginary components of the TG and PE signals are defined by reference to the pure buffer solution, which is taken to possess a fully dispersive (imaginary) signal phase because it is transparent to visible light. The phases are calibrated by measuring TG signal fields with the buffer, then exchanging the sample reservoir with APC solution without moving the flow cell. With the known phase of the TG signal for APC, the PE signal phase is readily obtained using the projection slice theorem of Fourier transforms.[62] Two-dimensional PE signals are integrated over the ω_τ dimension (i.e., Fourier transform of τ delay), and the phase of this projection is adjusted for agreement with the TG signal phase. Earlier investigations successfully use this same phasing procedure.[52,63]

III. Modeling Spectroscopic Signals

This section presents a theoretical model that will be used to interpret all linear and nonlinear spectroscopic measurements in this paper. The foundation of the model is taken from sections 5.1 and 5.2 of ref 25, where the cumulant expansion of Gaussian fluctuations (CGF) yields line broadening functions and incoherent exciton transport rates. The CGF model is chosen because of its demonstrated success in the simulation of correlated line broadening dynamics.[18] Experimentally detected signals in the following sections will show that vibronic coupling is an important component of the optical response of APC. Below, the model of ref 25 is supplemented to capture effects of vibronic coupling.

IIIA. Description of Correlated Line Broading in the Basis of Pigment Sites. The Frenkel exciton model with CGF line broadering dynamics has been presented in full detail elsewhere.[25,26] Here we present some of the fundamental equations to establish notation and aspects of the model specific to the present treatment. The equations are written for general

application to systems with arbitrary numbers of molecules. The Hamiltonian of the pigment complex is partitioned into three components as

$$H = H_{\text{Sys}} + H_{\text{Bath}} + H_{\text{Sys-Bath}} \tag{1}$$

where the system Hamiltonian is given by

$$H_{\text{Sys}} = \sum_m^N E_m B_m^\ddagger B_m + \sum_m^N \sum_{n \neq m}^N J_{mn} B_m^\ddagger B_n \tag{2}$$

Here, E_m is the energy gap of molecule m; J_{mn} is the electrostatic coupling between molecules m and n; and N is the number of molecules in the complex. The CGF treatment of line broadening describes the time scale and magnitude of fluctuations in E_m with the parameters Λ_{mm}^{-1} and Δ_{mm}, respectively. Correlated fluctuations at different pigment sites are found with the Cauchy−Schwartz inequality[18]

$$\Delta_{mn}^2 = \eta_{mn} \Delta_{mm} \Delta_{nn} \tag{3}$$

where η_{mn} interpolates between the fully correlated, $\eta_{mn} = 1$, and anticorrelated, $\eta_{mn} = -1$, limits. To minimize the number of adjustable parameters in this paper, we assume that all Λ_{mn} and Δ_{mn} possess the same ratio $\kappa = \Lambda_{mn}/\Delta_{mn}$. Therefore, fluctuations at a pair of molecular sites, m and n, are fully described with four parameters: Δ_{mm}, Δ_{nn}, η_{mn}, and κ. Our model calculations further assume the overdamped Brownian oscillator line broadening function in the high-temperature limit

$$g'_{mn}(t) = g'_{nm}(t) = \frac{1}{\kappa^2}\left(1 - i\frac{\kappa\Delta_{mn}}{2k_B T}\right)[\exp(-\Lambda_{mn}|t|) + \Lambda_{mn}t - 1] \tag{4}$$

IIIB. Transforming Line Broadening Functions into the Exciton Basis. The Hamiltonian matrix is diagonalized in a basis of zero, one, and two excitations yielding a ground state, N single exciton states, and $N(N - 1)/2$ double exciton states.[21,25,26] Eigenvectors of the single and double exciton states are, respectively, written as

$$|a\rangle = \sum_m^N \phi_{am}|m\rangle \tag{5}$$

and

$$|c\rangle = \sum_{m=1}^{N-1} \sum_{n+1}^N \xi_{c,mn}|m\rangle|n\rangle \tag{6}$$

This paper reserves the dummy indices a and b for single exciton states and c for the double exciton manifold. Transformation of the line broadening functions from the local to exciton basis is accomplished using

$$g'_{ab}(t) = g'_{ba}(t) = \sum_{n=1}^N \sum_{m=1}^N \phi_{am}^2 \phi_{bn}^2 g'_{mn}(t) \tag{7}$$

$$g'_{ac}(t) = g'_{ca}(t) = \sum_{n=1}^{N} \sum_{m=1}^{N-1} \sum_{k=m+1}^{N} \phi_{a,m}^2 \xi_{c,nk}^2 [g'_{mn}(t) + g'_{mk}(t)] \tag{8}$$

$$g'_{cd}(t) = g'_{dc}(t) = \sum_{m=1}^{N-1} \sum_{n=m+1}^{N} \sum_{k=1}^{N-1} \sum_{l=k+1}^{N} \xi_{c,mn}^2 \xi_{d,kl}^2 [g'_{mk}(t) + g'_{ml}(t) + g'_{nk}(t) + g'_{nl}(t)] \tag{9}$$

where the symmetrized line broadening function is defined as $g_{mn}(t) \equiv g'_{mn}(t) + g'_{nm}(t).$[24] Damping imposed by loss of correlation between a pair of single exciton states is described by $g_{ab}(t)$; $g_{ac}(t)$ corresponds to single exciton a and double exciton c; $g_{cd}(t)$ refers to double excitons c and d.

IIIC. Nonlinear Response Functions. Under perfect phase-matching conditions, the signal field is related to the third-order polarization by

$$E_S(t) = \frac{i2\pi l \omega_t}{n(\omega_t)c} P^{(3)}(t) \tag{10}$$

where $n(\omega_t)$ is the refractive index; l is the sample thickness; and c is the speed of light. The polarization, $P^{(3)}(t)$, is induced with three applied fields, E_j, which can be written as[62]

$$E_j(t) = \varepsilon(t - \bar{\tau}_j)\cos[\omega_j(t - \bar{\tau}_j)] \tag{11}$$

where $\varepsilon(t - \bar{\tau}_j)$ is a Gaussian envelope centered at time $\bar{\tau}_j$ (see Figure 2) and ω_j is the carrier frequency of the field. The Feynman diagrams shown in Figure 3 represent the 10 dominant terms in the nonlinear response function, where all terms assume that the two "pump" pulses, E_1 and E_2, interact with the sample before the "probe" pulse, E_3.[25] This assumption is inherent to the "doorway−window" treatment of exciton transport introduced below.

This paper finds that the accurate fitting of spectroscopic signals for APC must account for vibronic coupling. Vibronic structure is described ad hoc by adding two nuclear modes to the exciton basis. Below it is shown that, although the vibronic manifold is introduced in the exciton basis, the model still yields a microscopic interpretation because the vibrations are localized to the phycocyanobilin pigments comprising the dimers of APC. Response functions for terms in the first two rows of Figure 3 are given in ref 25. To make clear the specifics of the present treatment, we demonstrate how vibronic levels and electric field polarization effects are addressed using the $R_1(t_1, t_2, t_3)$ term as an example. The expression
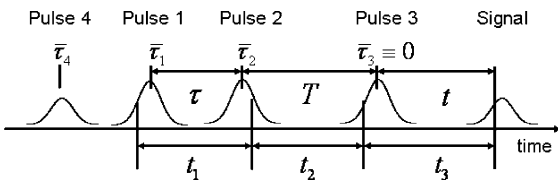
Figure 2. Pulse sequence used for TG and PE spectroscopies. Arrival times of the four pulses (at their peaks) are represented by $\bar{\tau}_i$. The delays, $\tau = \bar{\tau}_2 - \bar{\tau}_1$ and $T = \bar{\tau}_3 - \bar{\tau}_2$, are experimentally controlled. Intervals between field−matter interaction times are given by t_1, t_2, and t_3. Pulse 4 is a reference field (i.e., local oscillator) used for interferometric signal detection.

$$R_1(t_1, t_2, t_3) = \sum_{ab} \mu_{ag}^2 \mu_{bg}^2 \exp\left(-i\omega_{ag}t_1 + i\omega_{ba}t_2 - i\omega_{ag}t_3 - \frac{1}{2}f_1(t_1, t_1 + t_2, t_1 + t_2 + t_3, 0)\right) \tag{12}$$

is obtained directly from eq 5.26 in ref 25, where a sum of line broadening functions is obtained by expansion of $f_1(t_1, t_1 + t_2, t_1 + t_2 + t_3, 0)$, using eq 5.27. Electric field polarizations and vibronic coupling are incorporated by rewriting eq 12 as

$$R_1(t_1, t_2, t_3) = \sum_{ab} \langle \alpha_{gb}\beta_{ag}\gamma_{bg}\chi_{ga} \rangle Z_{ab}^1(t_1, t_2, t_3) \times$$
$$\exp\left(-i\omega_{ag}t_1 - i\omega_{ab}t_2 - i\omega_{ag}t_3 - \frac{1}{2}f_1(t_1, t_1 + t_2, t_1 + t_2 + t_3, 0)\right) \tag{13}$$

The orientational factor, $\langle \alpha_{gb}\beta_{ag}\gamma_{bg}\chi_{ga} \rangle$, is given in Appendix A, and vibronic coupling is described by

$$Z_{ab}^1(t_1, t_2, t_3) =$$
$$F_a^{00}F_b^{00} + \sum_{v=1}^{2} F_{av}^{01}F_b^{00} \exp[-(i\omega_v + k_v)(t_1 + t_2 + t_3)] +$$
$$F_a^{00}F_{bv}^{01} \times \exp[(i\omega_v - k_v)t_2] + \delta_{ab}F_{av}^{01}F_{bv}^{00} \times$$
$$\exp(-i\omega_v t_1 - k_v(t_1 + t_2)) \times [\exp(-i\omega_v t_3 - k_v t_3) +$$
$$(\exp(k_v t_2) - 1)] \tag{14}$$

where ω_v is the frequency of mode v; F_a^{00} is the Franck−Condon factor coupling the ground state to the electronic origin of
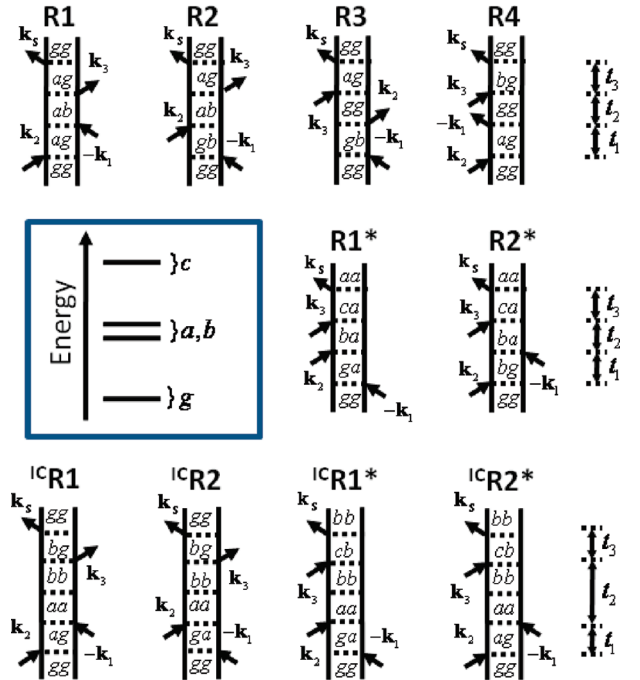
Figure 3. Feynman diagrams for dominant terms in the transient grating and photon echo spectroscopies in this paper. The dummy indices a and b are used for single exciton states, whereas c is reserved for the double exciton manifold. The superscript IC used in the bottom row denotes incoherent exciton transport. Terms in the nonlinear response function corresponding to these diagrams are presented in Section IIIC and Appendix B.

Light-Harvesting Dimers of Allophycocyanin

J. Phys. Chem. B, Vol. xxx, No. xx, XXXX **E**

excited state a; F_{av}^{01} is the Franck−Condon factor corresponding to a process in which photoexcitation initiates at the ground state and terminates in the first excited vibronic level of electronic state a and mode ν; and k_ν represents the inverse lifetime of mode ν (i.e., vibrational cooling rate). Equation 14 keeps only the dominant terms in which at least two field matter interactions couple the electronic origins of the ground and excited states. Neglect of higher-order terms is appropriate for systems, such as APC, in which the 0−0 transitions possess the largest Franck−Condon factors. Signal components evolving as excited state nuclear coherences in t_2 can also be envisioned for diagrams in which $a = b$ and/or $a \neq b$.[64,65] However, the TG and PE signals of APC are well-captured without this additional complexity because terms with four field−matter interactions coupling the electronic origins of g and a (or g and b) possess the largest nonlinearities.

The physical significance of $Z_{ab}^1(t_1,t_2,t_3)$ is made clear by considering it as the sum of three terms. The first term, which is simply equal to $F_a^{00}F_b^{00}$, represents a sequence in which all four field−matter interactions couple the electronic origins (i.e., 0−0 transitions). The second term accounts for all field−matter interaction sequences evolving in a vibronic coherence during the t_2 interval. Finally, the third term, which is linear in the delta function, δ_{ab}, populates the first vibronic level of mode ν at $t_2 = 0$, then relaxes to the electronic origin at the rate k_ν. This term captures the short and long time limits of intramolecular nuclear relaxation by ensuring that stimulated emission occurs from hot vibronic states at short t_2 and from the electronic origins of the excited states at long t_2. Expressions for the terms in the response function corresponding to the five other diagrams in the first two rows of Figure 3 are given in Appendix B.

The CGF model describes fluctuations of the exciton energies and captures essential aspects of spectroscopic line shapes. However, fluctuations in the exciton couplings are needed for simulation of exciton transport. The doorway−window treatment of the nonlinear response, which is valid for well-separated pump and probe pulses, describes line broadening and population transfer on the same footing.[66] The doorway−window model is appropriate for APC because the dominant population transfer channel occurs with a time constant over 18 times larger than the experimental laser pulse duration. For convenience, the response function is partitioned into rephasing and non-rephasing terms. The rephasing, S_{OD}^{RP}, and nonrephasing, S_{OD}^{NRP}, components of the response function are, respectively, given by

$$S_{OD}^{RP}(t_1, t_2, t_3) = \sum_{ab} [W_{ab}^{ESE}(t_3) - W_{ab}^{ESA}(t_3)] \times$$
$$D_a(-t_1)[G_{ba}(t_2) - 1] - S_D^{RP}(t_1, \infty, t_3) \quad (15)$$

and

$$S_{OD}^{NRP}(t_1, t_2, t_3) = \sum_{ab} [W_{ab}^{ESE}(t_3) - W_{ab}^{ESA}(t_3)] \times$$
$$D_a(t_1)[G_{ba}(t_2) - 1] - S_D^{NRP}(t_1, \infty, t_3) \quad (16)$$

where the subscript, OD, refers to off-diagonal elements of the Hamiltonian (i.e., interexciton couplings). In $S_{OD}^{RP}(t_1,t_2,t_3)$ [$S_{OD}^{NRP}(t_1,t_2,t_3)$], the terms linear in the window functions, $W_{ab}^{ESE}(t_3)$ and $W_{ab}^{ESA}(t_3)$, respectively, correspond to the $^{IC}R2$ and $^{IC}R1^*$ [$^{IC}R1$ and $^{IC}R2^*$] terms in Figure 3. The doorway function is written as

$$D_a(t_1) = \exp[-i\omega_{ag}t_1 - g_{aa}(t_1)]\{F_a^{00} +$$
$$\sum_{\nu=1}^2 F_{av}^{01} \exp(-i\omega_\nu t_1 - k_\nu|t_1|)\} \quad (17)$$

where the vibronic manifold is consistent with that used for $Z_{ab}^1(t_1,t_2,t_3)$ in eq 14. The window functions are given by

$$W_{ab}^{ESE}(t_3) = \langle\alpha_{ga}\beta_{ag}\gamma_{bg}\chi_{gb}\rangle\exp[-i\omega_{bg}t_3 - g_{bb}(t_1) +$$
$$2i\lambda_{bb}t_3]\{F_b^{00} + \sum_{\nu=1}^2 F_{bv}^{01} \exp(i\omega_\nu t_3 - k_\nu t_3)\} \quad (18)$$

and

$$W_{ab}^{ESA}(t_3) = \sum_c \langle\alpha_{ga}\beta_{ag}\gamma_{cb}\chi_{bc}\rangle\exp[-i\omega_{cb}t_3 - g_{bb}(t_3) -$$
$$g_{cc}(t_3) + 2g_{cb}(t_3) + 2i(\lambda_{cb} - \lambda_{bb})t_3] \quad (19)$$

where the vibronic structure of $W_{ab}^{ESE}(t_3)$ is consistent with that of $Z_{ab}^1(t_1,t_2,t_3)$ and $D_a(t_1)$. The linear absorbance and fluorescence spectra impose valuable constraints for parametrization of the vibronic couplings strengths, F_{av}. However, the experimental data presented here do not provide information sufficient to determine the vibronic couplings associated with transitions between the single and double exciton manifolds. For this reason, vibronic coupling effects are neglected in $W_{ab}^{ESA}(t_3)$.

Expressions for the response functions are convoluted with the applied electric fields to obtain the third-order polarization as

$$P^{(3)}(t) = \int_0^\infty dt_1 \int_0^\infty dt_2 \int_0^\infty dt_3 [S_D^{NRP}(t_1, t_2, t_3) +$$
$$S_{OD}^{NRP}(t_1, t_2, t_3)] \times E_3(t - t_3)E_1^*(t - t_3 - t_2)E_2(t - t_3 - t_2 -$$
$$t_1) + [S_D^{RP}(t_1, t_2, t_3) + S_{OD}^{RP}(t_1, t_2, t_3)] \times E_3(t - t_3)E_2(t -$$
$$t_3 - t_2)E_1^*(t - t_3 - t_2 - t_1) \quad (20)$$

where the rephasing and nonrephasing terms associated with (diagonal) energy level fluctuations are given by

$$S_D^{RP}(t_1, t_2, t_3) = R_2(t_1, t_2, t_3) + R_3(t_1, t_2, t_3) - R_1^*(t_1, t_2, t_3)$$
$$(21)$$

$$S_D^{NRP}(t_1, t_2, t_3) = R_1(t_1, t_2, t_3) + R_4(t_1, t_2, t_3) - R_2^*(t_1, t_2, t_3)$$
$$(22)$$

Equation 20 will be used to model transient grating and photon echo experiments. The model calculations below constrain parameters by simultaneous fitting of absorbance and fluorescence spectra, which are calculated with

$$\sigma_A(\omega) = \sum_{a=1}^N \mu_{ag}^2 \int_0^\infty dt\{F_a^{00} + \sum_{\nu=1}^2 F_{av}^{01} \exp(-i\omega_\nu t)\} \times$$
$$\exp\left[i(\omega - \omega_{ag})t - \frac{1}{2}g_{aa}(t)\right]\Phi_a(t) \quad (23)$$

and

$$\sigma_F(\omega) = \sum_{a=1}^{1} \mu_{ag}^2 \int_0^\infty dt \{ F_a^{00} + \sum_{\nu=1}^{2} F_{a\nu}^{01} \exp(i\omega_\nu t) \} \times$$

$$\exp\left[i(\omega - \omega_{ag})t - \frac{1}{2} g_{aa}^*(t) \right] \Phi_a(t) \quad (24)$$

where $\Phi_a(t)$ accounts for lifetime broadening and is obtained by summing the Green function, $G_{ba}(t)$, over all population transfer channels as

$$\Phi_a(t) = \sum_b G_{ba}(t) \quad (25)$$

The Green function used here is parametrized phenomenologically as

$$G_{12}(t) = 0.35 \exp(-t/35) + 0.65 \exp(-t/280) \quad (26)$$

and population transfer from the lower to higher energy exciton state is neglected because of the large energy gap between the exciton states. Section V discusses why this phenomenological parametrization of $G_{12}(t)$ is performed in lieu of modified Redfield theory.[66,67]

IV. Results and Discussion

IVA. Linear Absorption and Fluorescence Spectra. Fits to the linear absorption and fluorescence spectra of APC are presented in Figure 4, where parameters of the model are given in Table 1. The spectra are quite similar to those found by Edington et al.[32] The line shape of the $e+$ transition exhibits well-resolved vibronic structure, whereas vibronic transitions are obscured by lifetime broadening in the $e-$ band. Resonance Raman measurements show that many vibrational modes couple to the excitations.[43,44] However, fitting of the present experimental data is accomplished with two high-frequency modes at 800 and 1500 cm^{-1}. In essence, this treatment sums the intramolecular reorganization energy for all displaced modes with similar frequencies onto the two coordinates with the goal of minimizing adjustable parameters (see Supporting Information). It should be emphasized that this pair of measurements only partially constrains the model parameters. The nonlinear spectroscopies discussed below are also taken into account. For example, the Green function that causes lifetime broadening of the $e-$ band [see eq 26] is parametrized to simultaneously fit the transient grating signal spectra and anisotropies presented in the following section.

IVB. Dynamics in the Transient Grating Signal Spectrum. The transient grating (TG) measurements shown in Figure 5 separate real (absorptive) and imaginary (dispersive) signal components for both ZZZZ and ZZXX tensor elements. This tensor notation denotes the electric field polarizations involved in the sequence of four field−matter interactions (see Appendix A). The real signal components provide information equivalent to a conventional pump−pump experiment (i.e., transient absorption), whereas the interpretation of dispersive signal components is more complicated. In the limit of laser pulses with infinite bandwidths, the real and imaginary signals are (exactly) related by a Kramers−Kronig transformation. However, because finite bandwidth pulses are actually used, the imaginary signal components in Figure 5 report on dynamics taking place outside of the spectral window defined by the probe
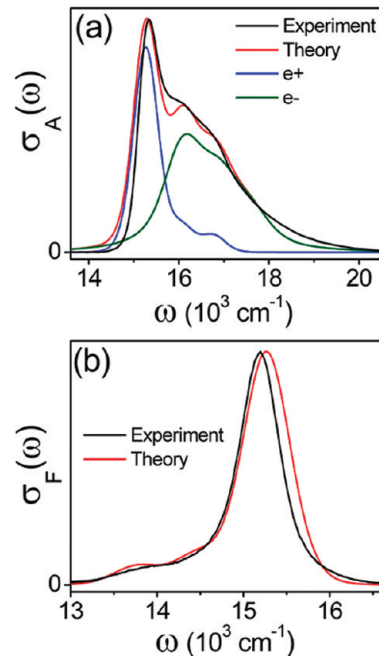

Figure 4. (a) Experimental (black) and theoretical (red) linear absorption spectra. Also shown are the line shapes of the transitions to the $e+$ (blue) and $e-$ (green) single exciton states. (b) Experimental (black) and theoretical (red) fluorescence spectra. Calculations use the parameters in Table 1.

TABLE 1: Parameters of the Spectroscopic Model

parameter	value
$^a E_1/hc$	15300 cm^{-1}
$^a E_2/hc$	16060 cm^{-1}
J_{12}	−163 cm^{-1}
Δ_{11}	450 cm^{-1}
Δ_{22}	560 cm^{-1}
η_{12}	0
κ	0.25
ω_ν ($\nu = 1$)	800 cm^{-1}
ω_ν ($\nu = 2$)	1500 cm^{-1}
$^b F_a^{00}$ ($a = 1$)	2.05
$^b F_a^{00}$ ($a = 2$)	0.64
$F_{a\nu}^{01}$ ($a = 1, \nu = 1$)	0.24
$F_{a\nu}^{01}$ ($a = 1, \nu = 2$)	0.16
$F_{a\nu}^{01}$ ($a = 2, \nu = 1$)	0.38
$F_{a\nu}^{01}$ ($a = 2, \nu = 2$)	0.09
k_ν^{-1} (all ν)	50 fs
$\omega_1 = \omega_2 = \omega_3$	15940 cm^{-1}

^{a} Energy gap of pigment in eq 2. ^{b} $a = 1$ and $a = 2$, respectively, denote the $e+$ and $e-$ excitons.

laser spectrum.[63,68,69] Therefore, the dynamics measured at different signal phase angles provide complementary information.

The real TG signals shown in Figure 5 display a red-shift in the signal spectrum taking place within the first several hundred femtoseconds. The red-shift observed in the real signal component is consistent with previous pump−probe measurements for APC in which the dynamics were assigned to both electronic and nuclear relaxation.[32,40,42] By contrast, significant red-shifting is not found in the imaginary signal components. Rather, the imaginary amplitude at $\omega_t = 15\,400$ cm^{-1} rises on a time scale similar to that with which the real spectrum red-shifts. This rise in amplitude is quite significant with an increase of more than a factor of 5 between $T = 0$ and $T = 0.5$ ps. In addition to population dynamics of the excitons, the imaginary signal component possesses enhanced sensitivity to the Raman response of the surrounding protein environment and solvent (i.e.,
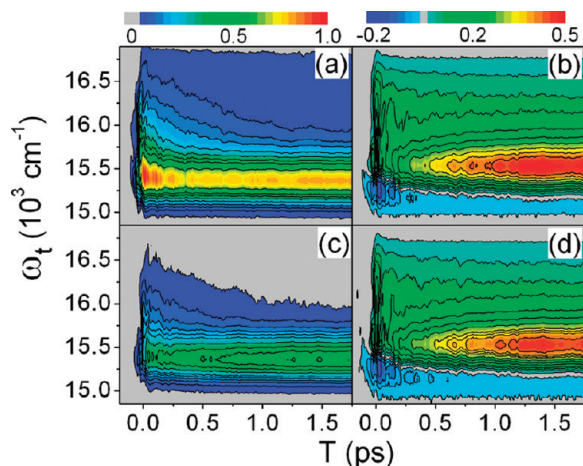
Light-Harvesting Dimers of Allophycocyanin

J. Phys. Chem. B, Vol. xxx, No. xx, XXXX **G**

Figure 5. Real (a), (c) and imaginary (b), (d) parts of the transient grating signal field measured for the ZZZZ (a), (b) and ZZXX (c), (d) tensor elements. Amplitudes of the four spectra are normalized to the same value and can be directly compared.
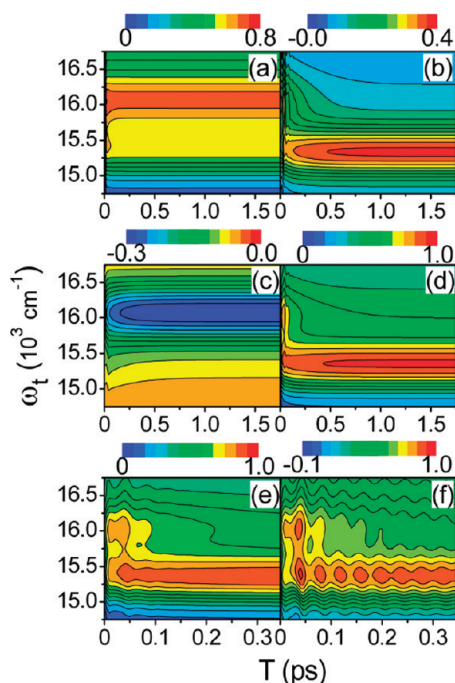

Figure 6. Panels (a)−(c) present the real part of calculated transient grating signals for terms: (a) R3, R4; (b) R1, R2, ^{IC}R1, ^{IC}R2; (c) R1*, R2*, ^{IC}R1*, ^{IC}R2*. Panels (d)−(f) are computed using eq 20, where (d) and (e) show the same calculation plotted on different time scales. The parameters of Table 1 are used with the exception that panel (f) sets the correlation parameter, η, equal to 1 (see eq 3).

as in an optical Kerr effect).[70,71] We make no attempt to extract this information here but focus on coherent dynamics found in the imaginary signal component in section IVD.

The model calculation shown in Figure 6 suggests that both electronic and nuclear relaxation contribute to the red-shift measured in the transient grating signal spectrum. Interpretation is facilitated by decomposing the signal into three contributions: ground state bleach (GSB); excited state emission (ESE); excited state absorption (ESA). Figure 6a shows that the GSB component is essentially independent of the pulse delay T, whereas the ESE and ESA terms, respectively, shift to lower and higher frequencies with increasing T. It is essential that interference between the ESE and ESA terms is considered to understand the dynamics in the total signal spectrum shown in Figure 6d.
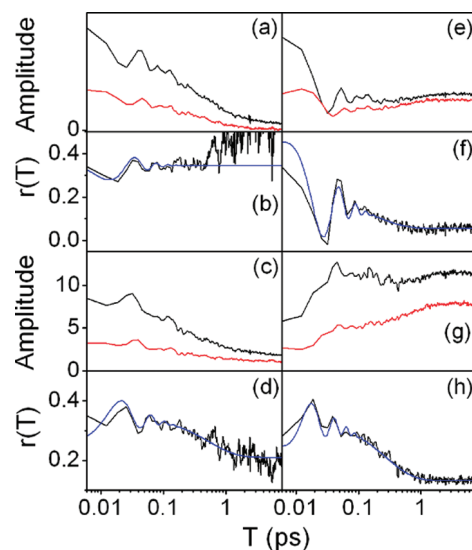

Figure 7. Tensor elements measured with ZZZZ (black) and ZZXX (red) tensor elements along with the corresponding anisotropies are shown in four pairs of panels: (a),(b); (c),(d); (e),(f); (g),(h). Panels (e) and (f) represent the imaginary part of the transient grating signal field, whereas all other data correspond to the real component. The panels in all rows use the same scale and can be compared. Signal detection frequencies for the four pairs of panels are: (a),(b) 16 000 cm^{-1}; (c),(d) 15 750 cm^{-1}; (e),(f) 16 000 cm^{-1}; (g),(h) 15 270 cm^{-1}. Fitting parameters are given in Table 2.

The excited state emission terms in the response function radiate as hot vibronic states with spectra resembling the line shapes shown in Figure 4a at $T = 0$, whereas the signals converge to mirror images of the absorption spectrum when T is long compared to the vibrational cooling time of 50 fs. Internal conversion between $e-$ and $e+$ is also partly responsible for the red-shift in the signal field, where the 35 fs relaxation channel represents the major contribution. Electronic relaxation dominates the response at $T > 100$ fs because the internal conversion rate possesses a significant (65%) 280 fs component.

Figures 6e and 6f present TG signals computed without ($\eta = 0$) and with ($\eta = 1$) fully correlated fluctuations at the individual pigment sites. Full correlation gives rise to a long-lived electronic coherence between the $e+$ and $e-$ exciton states; this coherence manifests as oscillations in the signal amplitude with a period of 40 fs. By contrast, recurrences in the signal amplitude are not observed with $\eta = 0$. In fact, indistinguishable signals are obtained with $0 < \eta < 0.5$ (see Supporting Information). An essential finding of this model is that, with the exception of the coherent quantum beating dynamics shown in Figure 6f, spectroscopic signatures of exciton correlations are quite subtle and not readily detected with the present configurations of TG and PE spectroscopy. We parametrize the model with $\eta = 0$ on the basis of these calculations and the absence of electronic quantum beating in the measurements.

IVC. Incoherent Dynamics in the Transient Grating Signal Anisotropy. Analysis of electric field polarization effects is useful for distinguishing electronic population transfer from nuclear relaxation.[36,72−76] The anisotropy is calculated with real TG tensor elements using

$$r(T) = \frac{S_{ZZZZ}(T) - S_{ZZXX}(T)}{S_{ZZZZ}(T) + 2S_{ZZXX}(T)} \qquad (27)$$

We reiterate that the anisotropy computed with real TG signal components gives information equivalent to that obtained with

TABLE 2: Fits to Anisotropy Profiles in Figure 7

^{a}parameter	$^b\omega_t =$ 16000 cm^{-1}	$^b\omega_t =$ 15750 cm^{-1}	$^c\omega_t =$ 16000 cm^{-1}	$^b\omega_t =$ 15270 cm^{-1}
r_0	0.36	0.21	0.06	0.13
r_1	0	0.14	0.13	0.21
r_2	0.1	0.10	0.33	0.11
τ_1	—	550 fs	220 fs	280 fs
τ_2	35 fs	37 fs	36 fs	30 fs
ω	800 cm^{-1}	800 cm^{-1}	800 cm^{-1}	1450 cm^{-1}
φ	0.9 rad	2.9 rad	5.1 rad	1.4 rad

^{a} Fit to equation $r(T) = r_0 + r_1 \exp(-T/\tau_1) + r_2 \cos(\omega T + \varphi)\exp(-T/\tau_2)$. ^{b} Real component of signal. ^{c} Imaginary component of signal.

conventional pump−probe experiments. Figures 7a and 7b display the anisotropy at $\omega_t = 16\,000$ cm^{-1}. The signal amplitude decays significantly on the subpicosecond time scale, whereas the anisotropy remains at approximately 0.36 for $T < 0.5$ ps (see Table 2). The anisotropy in panel 7b measured at $T > 0.5$ ps is not meaningful due to limitations in the dynamic range of our instrument. Figures 7g and 7h present real TG tensor elements and the anisotropy measured at the low frequency edge of the signal spectrum, $\omega_t = 15270$ cm^{-1}. The signal amplitudes exhibit a rise concomitant with the red-shift shown in Figures 5a and 5c. The anisotropy decays with a 280 fs time constant, which is in exact agreement with that previously measured by Beck and co-workers (see Table 2).[28] Real TG signals detected at the intermediate frequency, $\omega_t = 15\,750$ cm^{-1}, are shown in Figures 7c and 7d. The anisotropy decays with the time constant of 550 fs which is almost twice that found at $\omega_t = 15\,270$ cm^{-1}. It is possible that population transfer and nuclear relaxation both contribute to the 550 fs time constant. In addition, the model calculations suggest that the dynamics measured at $\omega_t = 15\,750$ cm^{-1} are complicated by the interference between ESE and ESA (see Figure 7). Parameters in Table 2 describing coherences in the anisotropies are discussed in the following section.

The imaginary signal components detected at $\omega_t = 16\,000$ cm^{-1} are plotted primarily to emphasize the coherences discussed in the following section. However, the measured time constant of 220 fs deserves mention because it is in exact agreement with the time constant found using photon echo spectroscopy by Homoelle et al.[41] We believe that this time constant is most likely associated with internal conversion between the exciton states. For example, it may be that the 220 and 280 fs population transfer time constants represent distinct (heterogeneous) configurations of the dimer. The fact that this time constant is detected only in the imaginary signal component may also be significant. Reference 41 measures the photon echo signal intensity and therefore reports on dynamics occurring in both the real and imaginary components of the signal field.

The parameters of Table 1 capture the ω_t dependence of the anisotropies presented in Figure 7. Figure 8 overlays experimental and calculated anisotropies at three different pulse delays. The calculations are performed with and without the ESA terms to explain why the measured anisotropies do not decay significantly at $\omega_t > 15\,800$ cm^{-1}. The anisotropy is reasonably well-fit at $T = 0$, where the fast 35 fs component of the Green function in eq 26 is essential for obtaining an anisotropy of approximately 0.35 at $T = 0$. The effect of the ESA signal component becomes clear at $T = 200$ fs, where it suppresses decay in the anisotropy on the high frequency side of the signal spectrum. At $T = 3$ ps, experimental limitations prevent accurate measurement of the anisotropy at $\omega_t > 15\,800$ cm^{-1}. The measured anisotropy is also slightly smaller than that predicted
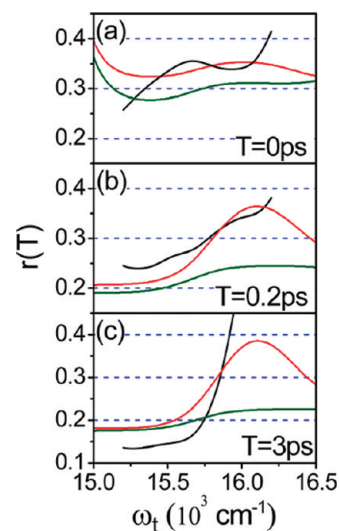

Figure 8. Experimental (black) and calculated (red and green) anisotropies with (a) $T = 0$ fs, (b) $T = 0.2$ fs, and (c) $T = 3$ ps. The anisotropies are computed with the real part of the signal field. Calculations represented with the red line use all terms in the response function, whereas the green line omits the excited state absorption terms R1*, R2*, ^{IC}R1*, and ^{IC}R2*.

by the model. One explanation for this discrepancy is that incoherent energy transfer between the initially photoexcited dimer and the two other dimers (see Figure 1a) contributes to the dynamics at $T > 1$ ps.

To summarize, contributions of electronic and nuclear relaxation to the TG signal spectrum and anisotropy have been investigated by comparing experimental and calculated signals. Important aspects of the measured signals include a red-shift in the signal spectrum taking place at $T < 500$ fs and a signal anisotropy for which the amount of depolarization increases with decreasing signal detection frequency, ω_t. The anisotropy decay occurs with time constants of 220, 280, and 550 fs. The 220 and 280 fs time constants agree with previous work and may represent electronic population transfer channels corresponding to different geometric configurations of the dimer. It is interesting that the present work obtains the same time constants as those found in ref 28 despite the broader distribution of photoexcited vibronic states produced by our 15 fs laser pulses. Apparently, this means that internal conversion occurs from the electronic origin of $e-$ because vibrational cooling is fast compared to these time constants. Interpretation of the 550 fs time constant is complicated by interference between the ESE and ESA signal components; nuclear relaxation may be an important contribution. We find that the sub-100 fs dynamics involve dephasing of electronic and nuclear coherences in addition to more than 35% of the total internal conversion between the $e-$ and $e+$ exciton states, whereas internal conversion dominates evolution in the TG signal spectrum at $T > 100$ fs.

IVD. Coherent Dynamics in the Transient Grating Signal Anisotropy. This section focuses on recurrences measured in the TG tensor elements and anisotropy. Nuclear coherences in APC have previously been investigated with high-quality pump−probe measurements employing 16 fs laser pulses.[42] However, recurrences in the anisotropy signals have not been reported. Table 2 summarizes fitting parameters for the anisotropy data in Figure 7 where all fits possess coherent components that damp in approximately 35 fs.

At the signal emission frequency $\omega_t = 16\,000$ cm^{-1}, a recurrence frequency of 800 cm^{-1} is found in both the real and
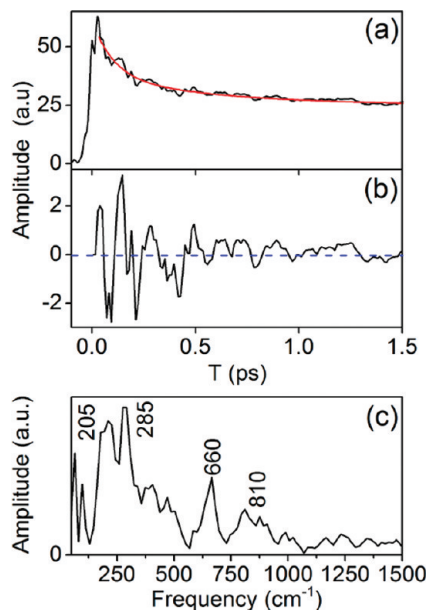
Light-Harvesting Dimers of Allophycocyanin

J. Phys. Chem. B, Vol. xxx, No. xx, XXXX **I**

Figure 9. (a) Real part of transient grating signal field measured with a 15 fs pump and probe pulses centered at 15 870 cm^{-1}. Signal is detected at 15 625 cm^{-1}. (b) Nuclear coherences are isolated by subtracting a decaying exponential function (red) from the data (black) in panel (a). (c) Absolute value of Fourier transform of residual signal in panel (b). The noise level in (c) is approximately 10% of the peak amplitude at 660 cm^{-1}.

imaginary signal components. Conventional transient absorption anisotropy corresponds to the real signal component. The anisotropy found with the imaginary signal components is displayed in Figure 7f because the large modulation depth gives strong support to the finding of anisotropic coherent dynamics. Signals detected at ω_t = 15 750 cm^{-1} are consistent with those at ω_t = 16 000 cm^{-1}.

The central issue in interpretation of the 800 cm^{-1} coherence measured at ω_t = 15 750 cm^{-1} and ω_t = 16 000 cm^{-1} is whether the coherence corresponds to a pair of electronic or nuclear states. To address this point, Figure 9 presents the Fourier transformation of a TG signal measured for the ZZZZ tensor element at 15 625 cm^{-1}, where we measure the greatest coherence amplitude. This Raman spectrum exhibits significant amplitude at 800 cm^{-1}. On the basis of resonance Raman studies for a related bilin chromophore, phytochrome, we assign the 800 cm^{-1} resonance to a hydrogen out-of-plane (HOOP) wagging mode analogous to those observed in retinal polyenes.[77−79] It is quite interesting that this is the only nuclear mode producing modulation in the anisotropies of Figure 7. Figure 9 clearly shows that lower frequency modes at 205 and 285 cm^{-1} couple more strongly to photoexcitation. However, these vibrations are apparently more symmetric in nature such that their contributions cancel in the numerator of eq 27.

Assignment of the dynamics to electronic coherence in APC is finally ruled out by the measurement of a recurrence with a frequency of 1450 cm^{-1} at ω_t = 15 270 cm^{-1}. Resonance Raman spectroscopy observes a transition at 1450 cm^{-1}.[44] The fact that the two coherence frequencies detected in the anisotropy agree with vibrational modes known to have large Franck−Condon factors leads us to conclude that the recurrences in the anisotropy correspond to impulsively excited vibrations. This finding has important implications for our interest in correlated line broadening. As shown in Figure 6, strongly correlated pigment fluctuations should promote long-lasting electronic coherences, which are readily detected with transient absorption anisotropy.[35]
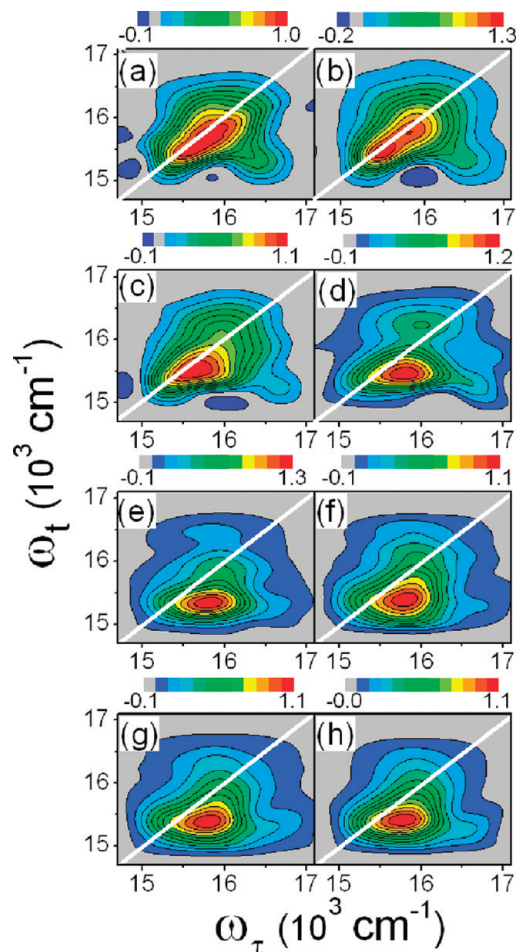

Figure 10. Real part of the experimental photon echo spectra measured at pulse delays, *T*: (a) 0 fs; (b) 10 fs; (c) 20 fs; (d) 30 fs; (e) 50 fs; (f) 70 fs; (g) 90 fs; (h) 120 fs. Pump (E_1 and E_3) and probe pulses (E_3 and E_4) are configured with magic angle polarizations. Amplitudes are scaled with respect to peak signal at *T* = 0 fs. The contour lines in each panel are linearly spaced.

IVE. Photon Echo Spectroscopy. Photon echo (PE) spectra obtained in the delay range *T* = 0−120 fs are presented in Figure 10. Inhomogeneity in the sample produces a peak shape elongated with respect to the diagonal, $\omega_\tau = \omega_t$, at *T* < 30 fs. This elongated peak shape quickly subsides as nuclear relaxation takes hold (e.g., solvation and dephasing of vibronic coherences). Most interesting is the presence of a fairly well-resolved cross peak located at ω_τ = 16 400 cm^{-1} and ω_t = 15 300 cm^{-1}. The model calculations shown in Figure 11 assign this cross peak to two signal generation mechanisms: (i) the first two field matter interactions produce a population in the 800 or 1500 cm^{-1} mode of state *e*+ which then relaxes to the electronic origin; (ii) excitation into the electronic origin of state *e*− is followed by internal conversion to state *e*+. The amplitude of the calculated cross peak is slightly underestimated and centered closer to ω_τ = 16 200 cm^{-1} and ω_t = 15 300 cm^{-1} at *T* = 0. Apparently, a small amount of relaxation not accounted for by the model takes place within the 18 fs time resolution of the experiment. However, the simulated cross peak intensity quickly grows, and the agreement between experiment and theory is quite good in the range *T* = 10−30 fs.

For *T* > 60 fs, the PE line shape exhibits increasing spectral width with decreasing ω_t. The time scale of relaxation in the peak shape is well-captured by the model. Overall, the dynamics in the PE spectrum reflect processes in which the excitation of
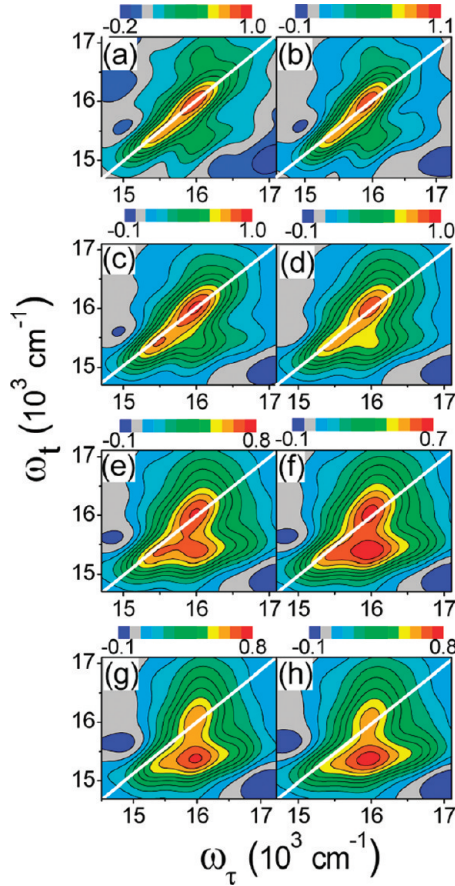
J *J. Phys. Chem. B, Vol. xxx, No. xx, XXXX*

Womick and Moran

Figure 11. Real part of calculated photon echo spectra measured at pulse delays, T: (a) 0 fs; (b) 10 fs; (c) 20 fs; (d) 30 fs; (e) 50 fs; (f) 70 fs; (g) 90 fs; (h) 120 fs. Pump (E_1 and E_3) and probe pulses (E_3 and E_4) are configured with magic angle polarizations. Amplitudes are scaled with respect to peak signal at $T = 0$ fs. Calculations use eq 20 and the parameters of Table 1. The contour lines in each panel are linearly spaced.

a broad distribution of initial states terminates in the electronic origin of the $e+$ exciton level. The most prominent internal conversion channel possesses a 280 fs time constant, whereas the PE spectrum changes little for $T > 120$ fs. Therefore, evolution of the PE spectrum found in Figure 10 must mainly reflect solvation and intramolecular nuclear relaxation within the $e+$ exciton level. The small Stokes shift between the absorption and fluorescence spectra of Figure 1c suggests that solvation is probably a minor contribution.

V. Conclusion

VA. Correlated Line Broadening. TG and PE measurements in this paper do not detect coherent quantum beating between the $e+$ and $e-$ excitons. Furthermore, we have shown that the present configurations of TG and PE are fairly insensitive to these dynamics because quantum beats in the TG signal are not observed unless the correlation parameter, η, is greater than 0.5; it should be noted that the PE line shapes are also indistinguishable for signals computed in the range $0 < \eta < 0.5$ (see Supporting Information). To better understand the present observations, we consider the initial amplitudes of the exciton–exciton cross-correlation function of APC[18]

$$\langle E_{e+}(0)E_{e-}(0)\rangle = \langle E_{e+}E_{e-}\rangle = \phi_{e+,1}^2\phi_{e-,1}^2\Delta_{11}^2 +$$
$$\phi_{e+,2}^2\phi_{e-,2}^2\Delta_{22}^2 + \eta_{12}[\phi_{e+,1}^2\phi_{e-,2}^2 + \phi_{e+,2}^2\phi_{e-,1}^2]\Delta_{11}\Delta_{22} \quad (28)$$

where

$$\langle E_{e+}E_{e-}\rangle/\text{cm}^{-2} = 20093 + \eta_{12}232378 \quad (29)$$

is obtained with the parameters of Table 1. The component of $\langle E_{e+}E_{e-}\rangle$ linear in η_{12} is 11.5 times larger than the first term under the condition of full correlation, $\eta_{12} = 1$. It is useful to compare this situation with that of a dimer possessing degenerate pigment energies where

$$\langle E_{e+}E_{e-}\rangle = \frac{1}{4}[\Delta_{11}^2 + \Delta_{22}^2] + \frac{\eta_{12}}{2}\Delta_{11}\Delta_{22} \quad (30)$$

is obtained. Here the third term is closer in magnitude to the sum of the first two. In fact, the autocorrelation functions and cross correlation functions possess equal weight when $\Delta_{11} = \Delta_{22}$, i.e., $2\langle E_{e+}E_{e-}\rangle = \Delta_{11}^2(1 + \eta_{12})$.

Together, eqs 28–30 suggest that the nondegenerate basis of APC facilitates the spectroscopic observation of electronic coherence if the pigment fluctuations of APC are indeed correlated. First, the term in eq 28 linear in η_{12} makes a significant contribution. Second, nondegeneracy of the pigment basis allows oscillator strength to be shared evenly between the two exciton transitions. Thus, an electronic coherence between $e+$ and $e-$ should be readily photoexcited and monitored with TG or PE. These factors promoting the observation of electronic coherences compete with fast dephasing dynamics imposed by vibrational cooling and electronic population transfer. On the basis of the present measurements and modeling, we can only conclude that $\eta_{12} < 0.5$. A forthcoming paper will address this issue with a nonlinear spectroscopy specially designed to isolate coherences between exciton states by suppressing the detection of electronic populations.[27]

VB. Importance of Promoting Modes. Geometry changes in the nuclear coordinates of the $e+$ and $e-$ exciton states are important because large Franck–Condon factors of "promoting modes" can potentially open efficient vibronic relaxation channels. Promoting modes are essential to explaining fast internal conversion in APC because the 827 cm^{-1} energy gap between exciton states is large compared to the characteristic frequency of the bath. For example, population transfer rates computed with a modified Redfield theory yield time constants of approximtely 13.2 ps (see Supporting Information), which is more than 50 times slower than the observed time scale. This slow rate reflects the fact that the spectral density of the solvent environment possesses little amplitude near 827 cm^{-1}. We suggest that a high frequency promoting mode of APC must enhance its internal conversion rate by accepting a portion of this excess energy.

One requirement for effective rate enhancement by way of a promoting mode is a large displacement in the coordinate for the $e+$ and $e-$ states. The displacement can be calculated using the vibronic coupling strengths in Table 1. For the 800 cm^{-1} mode, the vibronic coupling strength of the 0–0 transition is 8.3 and 1.7 larger than that of the 0–1 transition for the $e+$ and $e-$ states, respectively. These ratios correspond to dimensionless displacements (Huang–Rhys factors) of 0.63 (0.20) and 1.1 (0.63) for $e+$ and $e-$ (see Supporting Information). Thus, we estimate a dimensionless displacement of approximately 1.73 between the two exciton states. The rate enhancement can then be estimated by calculating the ratio of internal conversion rates found for cases in which the final state possesses either 0 or 1 quanta
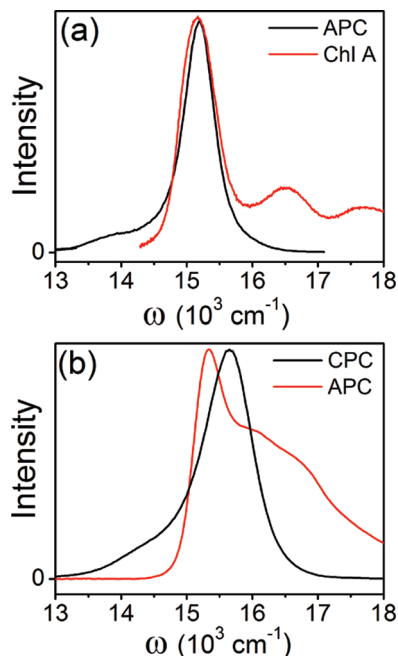
Light-Harvesting Dimers of Allophycocyanin

J. Phys. Chem. B, Vol. xxx, No. xx, XXXX **K**

Figure 12. Overlap of spectral line shapes for donor and acceptor pairs in the phycobilisome light harvesting antenna of cyanobacteria. (a) Fluorescence spectrum of allophycocyanin (APC, black) and absorption spectrum of chlorophyll A (Chl A, red). (b) Fluorescence spectrum of C-phycocyanin (CPC, black) and absorption spectrum of allophycocyanin (APC, red).

of energy in the 800 cm^{-1} mode of electronic state $e+$, where the transition is taken to initiate at the electronic origin of the $e-$ state.[80,81] The ratio, $k_{0\rightarrow1}/k_{0\rightarrow0}$, is given by

$$\frac{k_{0\rightarrow1}}{k_{0\rightarrow0}} = \frac{\Delta^2}{2} \exp\left[\frac{-(E_{00} - \hbar\omega_p)^2 + E_{00}^2}{2\sigma^2}\right] \quad (31)$$

where Δ is the dimensionless displacement in the nuclear coordinate; E_{00} is the 827 cm^{-1} energy gap between the electronic origins of the $e+$ and $e-$ states; σ is the bandwidth of the transition imposed with system−bath interactions; and the Gaussian line shape is assumed for convenience. The spectroscopic line widths are used to estimate a 275 cm^{-1} bandwidth, σ.

The point of eq 31 is only to obtain an order of magnitude estimate for the rate enhancement. Internal conversion rates of APC calculated with full rigor reach essentially the same conclusion.[42] Equation 31 yields a ratio $k_{0\rightarrow1}/k_{0\rightarrow0} = 137$, which puts the estimated internal conversion rate on the subpicosecond time scale. For example, a time constant of 96 fs is obtained if the rate enhancement factor of 137 is applied to the 13.2 ps time constant obtained by Redfield theory. On the basis of these calculations, we interpret the fast internal conversion dynamics of APC as proceeding through the vibronic relaxation channel of the 800 cm^{-1} HOOP vibrational mode shown in the Raman spectrum of Figure 9c (see section IVD). It should be noted that extremely rapid, promoting mode-assisted internal conversion is not unique to APC. Subpicosecond internal conversion rates across energy gaps close to 900 cm^{-1} have been found in various photosynthetic reaction centers.[35,82]

VC. Implications for Function of the Phycobilisome. Delivery of excitation energy from APC to the reaction center requires that energy absorbed by the $e-$ state transfers quickly

and efficiently to $e+$. Indeed, the excellent overlap between the fluorescence spectrum of APC and the absorption spectrum of the chlorophyll energy acceptor shown in Figure 12a suggests that the distribution of nuclear states in $e+$ is optimally configured for energy transfer to the reaction center. The parameters of Table 1 find that $e+$ and $e-$ exciton states are, respectively, 96% localized to $\beta84$ and $\alpha84$ pigments because the pigments comprising the dimer have nondegenerate energy levels. We suggest that exciton localization facilitates function of the phycobilisome in the following two ways. First, localization of the transition densities onto the individual pigments enhances the Franck−Condon factors essential to promoting mode-assisted internal conversion between $e-$ and $e+$. A second advantage to the nondegenerate basis is that oscillator strength distributes fairly evenly between the two exciton transitions. Overlap in the fluorescence emission spectrum of C-Phycocyanin (CPC) and the absorption spectrum of APC presented in Figure 12b suggests that the distribution of oscillator strength promotes energy transfer between this donor−acceptor pair by allowing the transition moments of both the $e+$ and $e-$ states of APC to couple with the energy donating state of CPC. By contrast, Förster energy transfer from CPC to the $e-$ state of APC would be less efficient if APC possessed degenerate pigments because the transition dipole connecting the ground state to $e-$ would have a smaller magnitude.

Appendix A. Tensor Elements for Electric Field Polarizations

This appendix presents the orientational part of the nonlinear response functions. The indices α, β, γ, and χ, respectively, correspond to the fields E_1, E_2, E_3, and E_S. For convenience, this orientational factor absorbs the four transition dipole magnitudes as

$$\langle\alpha_{ab}\beta_{cd}\gamma_{ef}\chi_{gh}\rangle = \frac{\mu_{ab}\mu_{cd}\mu_{ef}\mu_{gh}}{30}[\langle\cos\theta_{ef,gh}\cos\theta_{ab,cd}\rangle$$
$$\times (4\cos\theta_{\gamma\chi}\cos\theta_{\alpha\beta} - \cos\theta_{\beta\chi}\cos\theta_{\alpha\gamma} - \cos\theta_{\alpha\chi}\cos\theta_{\beta\gamma})$$
$$+ \langle\cos\theta_{cd,gh}\cos\theta_{ab,ef}\rangle(4\cos\theta_{\beta\chi}\cos\theta_{\alpha\gamma} - \cos\theta_{\gamma\chi}\cos\theta_{\alpha\beta}$$
$$- \cos\theta_{\alpha\chi}\cos\theta_{\beta\gamma}) + \langle\cos\theta_{ab,gh}\cos\theta_{cd,ef}\rangle(4\cos\theta_{\alpha\chi}\cos\theta_{\beta\gamma}$$
$$- \cos\theta_{\gamma\chi}\cos\theta_{\alpha\beta} - \cos\theta_{\beta\chi}\cos\theta_{\alpha\gamma})]$$
$$(A1)$$

Appendix B. Nonlinear Response Functions

This appendix presents expressions for response functions corresponding to four of the six Feynman diagrams in Figure 3. Section IIIC discusses the motivations for this model in the context of the $R_1(t_1,t_2,t_3)$ term. Response functions involving only the ground and single exciton electronic states are given by

$$R_2(t_1, t_2, t_3) = \sum_{ab} \langle \alpha_{gb}\beta_{ag}\gamma_{bg}\chi_{ga}\rangle Z^2_{ab}(t_1, t_2, t_3) \times$$
$$\exp\left(-i\omega_{gb}t_1 - i\omega_{ab}t_2 - i\omega_{ag}t_3 \right.$$
$$\left. - \frac{1}{2}f_1(0, t_1 + t_2, t_1 + t_2 + t_3, t_1)\right)$$
$$(B1)$$

$$R_3(t_1, t_2, t_3) = \sum_{ab} \langle \alpha_{gb}\beta_{bg}\gamma_{ag}\chi_{ga}\rangle Z^3_{ab}(t_1, t_2, t_3) \times$$
$$\exp\left(-i\omega_{gb}t_1 - i\omega_{ag}t_3 \right.$$
$$\left. - \frac{1}{2}f_1(0, t_1, t_1 + t_2 + t_3, t_1 + t_2)\right)$$
$$(B2)$$

$$R_4(t_1, t_2, t_3) = \sum_{ab} \langle \alpha_{ag}\beta_{ga}\gamma_{bg}\chi_{gb}\rangle Z^4_{ab}(t_1, t_2, t_3) \times$$
$$\exp\left(-i\omega_{ag}t_1 - i\omega_{bg}t_3 \right.$$
$$\left. - \frac{1}{2}f_1(t_1 + t_2 + t_3, t_1 + t_2, t_1, 0)\right)$$
$$(B3)$$

where the line broadening functions, $f_1(t_4, t_3, t_2, t_1)$, are given in ref 25 and vibronic coupling is described with

$$Z^2_{ab}(t_1, t_2, t_3) = F_a^{00}F_b^{00} + \sum_{\nu=1}^{2} F_a^{00}F_{b\nu}^{01} \times$$
$$\exp[(i\omega_\nu - k_\nu)(t_1 + t_2)] + F_{a\nu}^{01}F_b^{00} \times$$
$$\exp[-(i\omega_\nu + k_\nu)(t_2 + t_3)] +$$
$$\delta_{ab}F_{a\nu}^{01}F_{b\nu}^{00} \exp(i\omega_\nu t_1 - k_\nu(t_1 + t_2)) \times$$
$$[\exp(-i\omega_\nu t_3 - k_\nu t_3) + (\exp(k_\nu t_2) - 1)]$$
$$(B4)$$

$$Z^3_{ab}(t_1, t_2, t_3) = F_a^{00}F_b^{00} + \sum_{\nu=1}^{2} F_a^{00}F_{b\nu}^{01} \exp[i(\omega_\nu - k_\nu)t_1] +$$
$$F_{a\nu}^{01}F_b^{00} \exp[-i(\omega_\nu + k_\nu)t_3]$$
$$+ \delta_{ab}F_a^{00}F_{a\nu}^{01} \exp[i(\omega_\nu - k_\nu)t_2]$$
$$(B5)$$

$$Z^4_{ab}(t_1, t_2, t_3) = F_a^{00}F_b^{00} + \sum_{\nu=1}^{2} F_{a\nu}^{01}F_b^{00} \exp[-i(\omega_\nu +$$
$$k_\nu)t_1] + F_a^{00}F_{b\nu}^{01} \exp[-i(\omega_\nu + k_\nu)t_3]$$
$$+ \delta_{ab}F_a^{00}F_{a\nu}^{01} \exp[-i(\omega_\nu + k_\nu)t_2]$$
$$(B6)$$

Vibronic coupling functions for the ground state bleach terms, $Z^3_{ab}(t_1, t_2, t_3)$ and $Z^4_{ab}(t_1, t_2, t_3)$, sum over three terms evolving in coherences in either the t_1, t_2, or t_3 intervals. This model restricts the summation to the dominant terms in which at least two field matter interactions couple the electronic origins of the ground and excited states. This treatment is appropriate for systems, such as APC, in which the $0-0$ transitions possess the largest Franck−Condon factors.

The excited state absorption terms do not include vibronic structure due to limited experimental information. These terms

$$R_1^*(t_1, t_2, t_3) = \sum_{abc} \langle \alpha_{ga}\beta_{bg}\gamma_{cb}\chi_{ac}\rangle \exp\left(-i\omega_{ga}t_1 - i\omega_{ba}t_2 - \right.$$
$$\left. i\omega_{ca}t_3 - \frac{1}{2}f_2(t_1, t_1 + t_2, t_1 + t_2 + t_3, 0)\right) \quad (B7)$$

$$R_2^*(t_1, t_2, t_3) = \sum_{abc} \langle \alpha_{ga}\beta_{bg}\gamma_{cb}\chi_{ac}\rangle \exp\left(-i\omega_{bg}t_1 - i\omega_{ba}t_2 - \right.$$
$$\left. i\omega_{ca}t_3 - \frac{1}{2}f_2(0, t_1 + t_2, t_1 + t_2 + t_3, t_1)\right) \quad (B8)$$

are taken directly from section 5.1 of ref 25. Figure 3 reserves the indices a and b for single exciton states, whereas c is only used for double exciton states. Equation 5.28 in ref 25 does not use this convention. The $f_2(t_4, t_3, t_2, t_1)$ function used in eqs B7 and B8 is given by

$$f_2(t_4, t_3, t_2, t_1) = g_{aa}(t_{21}) + g_{cc}(t_{32}) + g_{bb}(t_{43}) - g_{ac}(t_{21}) -$$
$$g_{ac}(t_{32}) + g_{ac}(t_{31}) + g_{ab}(t_{32}) + g_{ab}(t_{41}) - g_{ab}(t_{31}) -$$
$$g_{ab}(t_{42}) - g_{cb}(t_{32}) - g_{cb}(t_{43}) + g_{cb}(t_{42}) \quad (B9)$$

Supporting Information Available: Intramolecular reorganization energies of the phycocyanobilin pigments are calculated. Figure 7 is presented on a linear scale. Transient grating and photon echo signals are compared with $\eta = 0$ and $\eta = 0.5$. This material is available free of charge via the Internet at http://pubs.acs.org.

References and Notes

(1) van Amerongen, H.; Valkunas, L.; van Grondelle, R. *Photosynthetic Excitons*; World Scientific: Singapore, 2000.
(2) Blankenship, R. E. *Molecular Mechanisms of Photosynthesis*; Blackwell Science Ltd.: Oxford, 2002.
(3) *Light Harvesting Antennas*; Green, B. R., Parson, W. W., Eds.; Kluwer Academic Publishers: Dordrecht, 2003; Vol. 13.
(4) Sundström, V.; Pullerits, T.; van Grondelle, R. *J. Phys. Chem. B* **1999**, *103*, 2327.
(5) Fleming, G. R.; Scholes, G. D. *Nature* **2004**, *121*, 4221.
(6) Parson, W. W. *Modern Optical Spectroscopy*; Springer-Verlag: Berlin, 2007.
(7) Soules, T. F.; Duke, C. B. *Phys. Rev. B* **1971**, *3*, 262.
(8) Parson, W. W. *Science* **2007**, *316*, 1438.
(9) Lee, H.; Cheng, Y.-C.; Fleming, G. R. *Science* **2007**, *316*, 1462.
(10) Rebentrost, P.; Mohseni, M.; Aspuru-Guzik, A. *J. Phys. Chem B* **2009**, *113*, 9942.
(11) Yu, Z. G.; Berding, M. A.; Wang, H. *Phys. Rev. E* **2008**, *78*, 0509902.
(12) Hennebicq, E.; Beljonne, D.; Curutchet, C.; Scholes, G. D.; Silbey, R. J. *J. Chem. Phys.* **2009**, *130*, 214505.
(13) Nazir, A. *Phys. Rev. Lett.* **2009**, *103*, 146404.
(14) Collini, E.; Scholes, G. D. *Science* **2009**, *323*, 369.
(15) Collini, E.; Scholes, G. D. *J. Phys. Chem. A* **2009**, *113*, 4223.
(16) Kimura, A.; Kakitani, T. *J. Phys. Chem. A* **2007**, *111*, 12042.
(17) Engel, G. S.; Calhoun, T. R.; Read, E. L.; Ahn, T. K.; Mancal, T.; Cheng, Y. C.; Blankenship, R. E.; Fleming, G. R. *Nature* **2007**, *446*, 782.
(18) Venkatramani, R.; Mukamel, S. *J. Chem. Phys.* **2002**, *117*, 11089.
(19) Demirdöven, N.; Khalil, M.; Tokmakoff, A. *J. Phys. Chem. A* **2001**, *105*, 8025.
(20) Pisliakov, A. V.; Mancal, T.; Fleming, G. R. *J. Chem. Phys.* **2006**, *124*, 234505.
(21) Cho, M. *Chem. Rev.* **2008**, *108*, 1331.
(22) Womick, J. M.; Miller, S. A.; Moran, A. M. *J. Phys. Chem. B* **2009**, *113*, 6630.
(23) Joo, T.; Jia, Y.; Yu, J.-Y.; Lang, M. J.; Fleming, G. R. *J. Chem. Phys.* **1996**, *104*, 6089.
(24) Mukamel, S. *Principles of Nonlinear Optical Spectroscopy*; Oxford University Press: New York, 1995.
(25) Abramavicius, D.; Mukamel, S. *Chem. Rev.* **2004**, *104*, 2073.

Light-Harvesting Dimers of Allophycocyanin

J. Phys. Chem. B, Vol. xxx, No. xx, XXXX **M**

(26) Abramavicius, D.; Palmieri, B.; Voronine, D. V.; Sanda, F. *Chem. Rev.* **2009**, *109*, 2350.

(27) Womick, J. M.; Miller, S. A.; Moran, A. M. *J. Phys. Chem. A* **2009**, *113*, 6587.

(28) Edington, M. D.; Riter, R. E.; Beck, W. F. *J. Phys. Chem.* **1995**, *99*, 15699.

(29) MacColl, R. *J. Struct. Biol.* **1998**, *124*, 311.

(30) Ying, L.; Sunney, X. *J. Phys. Chem B* **1998**, *102*, 10399.

(31) Brejc, K.; Ficner, R.; Huber, R.; Steinbacher, S. *J. Mol. Biol.* **1995**, *249*, 424.

(32) Edington, M. D.; Riter, R. E.; Beck, W. F. *J. Phys. Chem B* **1996**, *100*, 14206.

(33) McHale, J. *Molecular Spectroscopy*; Prentice Hall: Upper Saddle Creek River, NJ, 1999.

(34) Savikhin, S.; Buck, D. R.; Struve, W. S. *Chem. Phys.* **1997**, *223*, 303.

(35) Arnett, D. C.; Moser, C. C.; Dutton, P. L.; Scherer, N. F. *J. Phys. Chem. B* **1999**, *103*, 2014.

(36) Qian, W.; Jonas, D. M. *J. Chem. Phys.* **2003**, *119*, 1611.

(37) Milota, F.; Sperling, J.; Nemeth, A.; Kauffman, L. *J. Chem. Phys.* **2008**, *357*, 45.

(38) Pakoulev, A. V.; Rickard, M. A.; Meyer, K. A.; Kornau, K. M.; Mathew, N. A.; Thompson, D. E.; Wright, J. C. *J. Phys. Chem. A* **2006**, *110*, 3352.

(39) Pakoulev, A. V.; Rickard, M. A.; Mathew, N. A.; Kornau, K. M.; Wright, J. C. *J. Phys. Chem. A* **2007**, *111*, 6999.

(40) Edington, M. D.; Riter, R. E.; Beck, W. F. *J. Phys. Chem. B* **1997**, *101*, 4473.

(41) Homoelle, B. J.; Edington, M. D.; Diffey, W. M.; Beck, W. F. *J. Phys. Chem. B* **1998**, *102*, 3044.

(42) Zhang, J. M.; Shiu, Y. J.; Hayashi, M.; Liang, K. K.; Chang, C. H.; Gulbinas, V.; Yang, C. M.; Yang, T.-S.; Wang, H. Z.; Chen, Y.-T.; Lin, S. H. *J. Phys. Chem. A* **2001**, *105*, 8878.

(43) Szalontai, B.; Gombos, Z.; Csizmadia, V.; Csatorday, K.; Lutz, M. *Biochemistry* **1989**, *28*, 6467.

(44) Szalontai, B.; Gombos, Z.; Csizmadia, V.; Bagyinka, C.; Lutz, M. *Biochemistry* **1994**, *33*, 11823.

(45) Kneip, C.; Parbel, A.; Foerstendorf, H.; Scheer, H.; Siebert, F.; Hildebrandt, P. *J. Raman Spectrosc.* **1998**, *29*, 939.

(46) Mroginski, M. A.; Mark, F.; Thiel, W.; Hildebrandt, P. *Biophys. J.* **2007**, *93*, 1885.

(47) Doust, A. B.; Marai, C. N. J.; Harrop, S. J.; Wilk, K. E.; Curmi, P. M. G.; Scholes, G. D. *J. Mol. Biol.* **2004**, *344*, 135.

(48) Trebino, R. *Frequency Resolved Optical Gating: The Measurement of Ultrashort Laser Pulses*; Kluwer Academic Publishers: Boston, Dordrecht, London, 2000.

(49) Cowan, M. L.; Ogilvie, J. P.; Miller, R. J. D. *Chem. Phys. Lett.* **2004**, *386*, 184.

(50) Goodno, G. D.; Dadusc, G.; Miller, R. J. D. *J. Opt. Soc. Am. B* **1998**, *15*, 1791.

(51) Maznev, A. A.; Nelson, K. A.; Rogers, J. A. *Opt. Lett.* **1998**, *23*, 1319.

(52) Moran, A. M.; Maddox, J. B.; Hong, J. W.; Kim, J.; Nome, R. A.; Bazan, G. C.; Scherer, N. F. *J. Chem. Phys.* **2006**, *124*, 194904.

(53) Brixner, T.; Mancal, T.; Stiopkin, I. V.; Fleming, G. R. *J. Chem. Phys.* **2004**, *121*, 4221.

(54) Khurmi, C.; Berg, M. A. *J. Phys. Chem. A* **2008**, *112*, 3364.

(55) Underwood, D. F.; Blank, D. A. *J. Phys. Chem. A* **2003**, *107*, 956.

(56) Gundogdu, K.; Stone, K. W.; Turner, D. B.; Nelson, K. A. *Chem. Phys.* **2007**, *341*, 89.

(57) Kim, J.; Wong, C. Y.; Nair, P. S.; Fritz, K. P.; Kumar, S.; Scholes, G. D. *J. Phys. Chem. B* **2006**, *110*, 25371.

(58) Lepetit, L.; Chériaux, G.; Joffre, M. *J. Opt. Soc. Am. B* **1995**, *12*, 2467.

(59) Gallagher, S. M.; Albrecht, A. W.; Hybl, J. D.; Landin, B. L.; Rajaram, B.; Jonas, D. M. *J. Opt. Soc. Am. B* **1998**, *15*, 2338.

(60) Hybl, J. D.; Albrecht Ferro, A.; Jonas, D. M. *J. Chem. Phys.* **2001**, *115*, 6606.

(61) Khalil, M.; Demirdöven, N.; Tokmakoff, A. *J. Phys. Chem. A* **2003**, *107*, 5258.

(62) Jonas, D. M. *Annu. Rev. Phys. Chem.* **2003**, *54*, 425.

(63) Moran, A. M.; Park, S.; Scherer, N. F. *J. Phys. Chem. B* **2006**, *110*, 19771.

(64) Gallagher Faeder, S. M.; Jonas, D. M. *J. Phys. Chem. A* **1999**, *103*, 10489.

(65) Gallagher Faeder, S. M.; Jonas, D. M. *Phys. Rev. A* **2000**, *62*, 033820:1.

(66) Zhang, W. M.; Meier, T.; Chernyak, V.; Mukamel, S. *J. Chem. Phys.* **1998**, *7763*, 7763.

(67) Yang, M.; Fleming, G. R. *Chem. Phys.* **2002**, *282*, 163.

(68) Nelson, K. A.; Casalegno, R.; Miller, R. J. D.; Fayer, M. D. *J. Chem. Phys.* **1982**, *77*, 1144.

(69) Hybl, J. D.; Yu, A.; Farrow, D. A.; Jonas, D. M. *J. Phys. Chem. A* **2002**, *106*, 7651.

(70) Park, S.; Flanders, B. N.; Shang, X.; Westervelt, R. A.; Kim, J.; Scherer, N. F. *J. Chem. Phys.* **2003**, *118*, 3917.

(71) Goodno, G. D.; Astinov, V.; Miller, R. J. D. *J. Phys. Chem. B* **1999**, *103*, 603.

(72) Fleming, G. R. *Chemical Applications of Ultrafast Spectroscopy*; University Press: New York, 1986.

(73) Wynne, K.; Hochstrasser, R. M. *Chem. Phys.* **1993**, *171*, 179.

(74) Farrow, D. A.; Smith, E. R.; Qian, W.; Jonas, D. M. *J. Chem. Phys.* **2008**, *129*, 174509:1.

(75) Matro, A.; Cina, J. A. *J. Phys. Chem.* **1995**, *99*, 2568.

(76) Nagarajan, V.; Johnson, E. T.; Williams, J. C.; Parson, W. W. *J. Phys. Chem. B* **1999**, *103*, 2297.

(77) Palings, I.; Van den Berg, E. M. M.; Lugtenburg, J.; Mathies, R. A. *Biochemistry* **1989**, *28*, 1498.

(78) Andel, F., III; Murphy, J. T.; Haas, J. A.; McDowell, M. T.; van der Hoef, I.; Lugtenburg, J.; Lagarias, J. C.; Mathies, R. A. *Biochemistry* **2000**, *39*, 2667.

(79) Fodor, S. P.; Lagarias, J. C.; Mathies, R. A. *Biochemistry* **1990**, *29*, 11141.

(80) Freed, K. F. *Top. Appl. Phys.* **1976**, *15*, 23.

(81) Morse, M. D.; Puiu, A. C.; Smalley, R. E. *J. Chem. Phys.* **1982**, *78*, 3435.

(82) Jonas, D. M.; Lang, M. J.; Nagasawa, Y.; Joo, T.; Fleming, G. R. *J. Phys. Chem.* **1996**, *100*, 12660.